Hindawi Publishing Corporation
International Journal of Microwave Science and Technology
Volume 2015, Article ID 630131, 18 pages
http://dx.doi.org/10.1155/2015/630131

Research Article

The Spiral Coaxial Cable

I. M. Fabbri

Department of Physics, University of Milan, Via Celoria 16, 20133 Milan, Italy

Correspondence should be addressed to I. M. Fabbri; italomariofabbri@crfm.it

Received 18 September 2014; Revised 10 January 2015; Accepted 12 January 2015

Academic Editor: Kamya Yekeh Yazdandoost

A new concept of metal spiral coaxial cable is introduced. The solution to *Maxwell's* equations for the fundamental propagating *TEM* eigenmode, using a generalization of the *Schwarz-Christoffel* conformal mapping of the spiral transverse section, is provided together with the analysis of the impedances and the Poynting vector of the line. The new cable may find application as a medium for telecommunication and networking or in the sector of the Microwave Photonics. A spiral plasmonic coaxial cable could be used to propagate subwavelength surface plasmon polaritons at optical frequencies. Furthermore, according to the present model, the myelinated nerves can be considered natural examples of spiral coaxial cables. This study suggests that a malformation of the Peters angle, which determines the power of the neural signal in the *TEM* mode, causes higher/lower power to be transmitted in the neural networks with respect to the natural level. The formulas of the myelin sheaths thickness, the diameter of the axon, and the spiral g factor of the lipid bilayers, which are mathematically related to the impedances of the spiral coaxial line, can make it easier to analyze the neural line impedance mismatches and the signal disconnections typical of the neurodegenerative diseases.

1. Introduction

The coaxial cable invented by Heaviside [1] is a transmission line composed of an inner conductor surrounded by an insulating layer and an outer conducting shield. The inner and the outer conductors share the same geometrical axis.

Nowadays, there exist several types of transmission lines, the coaxial cables, the hollow waveguides (rectangular, circular, elliptical, and parallel plates [2, 3]), the two wires [3, 4], and the channel waveguides (buried, strip-loaded, ridge, rib, diffused, and graded-dielectric index [5]). The two-wire transmission line used in conventional circuits is inefficient for transferring electromagnetic energy at microwave frequencies because the fields are not confined in all directions, the energy escapes by radiation, and it has large copper losses due to its relatively small surface area.

On the other hand the larger surface area of the boundary makes in general the waveguides more efficient with respect to the coaxials on reducing the copper losses.

Dielectric losses in two wires and coaxial lines, caused by the heating of the insulation between the conductors, are also lower in waveguides. The insulation behaves as the dielectric of a capacitor and the breakdown of the insulation between the conductors of a transmission line is more frequently a problem than is the dielectric loss in practical applications [3].

Waveguides are also subject to the dielectric breakdown caused by the stationary voltage spikes at the nodes of the standing waves.

In spite of the dielectric in waveguides is air, it causes arcing which decreases the efficiency of energy transfer and can severely damage the waveguide.

The spiral coaxial cable (SCC) discussed in this paper has many advantages with respect to the other types of transmission lines; first of all the elm energy can be distributed efficiently over a larger area, reducing all the undesired aforementioned effects.

The power handling versus frequency is consequently higher for the metal spiral coaxial line (MSCC) with respect to the other lines.

The Microwave Photonics (MWP) [6], a new discipline that joins together the radio-frequency engineering and optoelectronics, represents the future in many civil and defense applications like speed of the digital signal processors, cable television, and optical signal processing.

The MSCC could become one of the key objects in the field of MWP for its characteristics in terms of both power handling and energy transfer efficiency.

Recently, it has also been demonstrated experimentally that metal coaxial waveguide nanostructures perform at

optical frequencies [7], opening up new research pursuits unexpected in the area of nanoscale waveguiding, field enhancement, imaging with coaxial cavities, and negative-index metamaterials [8].

Several different plasmonic waveguiding structures have been proposed such as metallic nanowires [9, 10], metal-dielectric-metal (MDM) structures [11], and metallic nanoparticle arrays [12] for achieving compact integrated photonic devices.

Most of these structures support a highly confined mode near the surface plasmon frequency [11]. This study could become the reference point to introduce the MSCC as a valid alternative to guide subwavelength surface plasmon polaritons (SPPs).

The extraordinary transmission of light through an array of subwavelength apertures, enhancement which arises from the coupling of the incident light with the SPPs through the surface grating in metal film [13], could result particularly efficiently on the spiral metal dielectric interface with periodic holes.

High sensitivity spiral biosensors and spiral photonic integrated circuits based on nonlinear surface plasmon polariton optics [14, 15] may be implemented.

The aim of this pioneering work on the SCC is to represent an initial landmark in the continuously growing sector of the microwave research.

The popularity of Video on Demand (VoD) and Over the Top Technology (OTT) services to access high definition videos over home interconnected devices of the hybrid fibre-coax (HFC) networks is driving the research toward more efficient and cost-effective cables. Particularly, the development of Converged Cable Access Platforms (CCAP) that combine video and data transmission supporting simultaneous network access of multiple users over a single coaxial cable is flourishing and sustaining the demand for new high speed transmission media.

In a metallic guide, the reflection mechanism responsible for confining the energy is due to the reflection from the conductors at the boundary [16], whose geometry is strictly related to the propagating modes.

Coaxial cables were designed to propagate high frequency radio signals. The principal constraints on performance of a coaxial are attenuation, thermal noise, and passive intermodulation noise (PIM).

In RF applications, the wave propagates essentially in the fundamental transverse electric magnetic (TEM) mode; that is, the electric and magnetic fields are both perpendicular to the direction of propagation.

In the ideal case, the conductors can be considered to have infinite conductivity and the TEM eigenmode is the basic propagating wave (see [17] page 110) along the transmission line.

Practical lines have finite conductivity, and this results in a perturbation or change of the TEM mode (see [18] page 119).

Above the cutoff frequency, transverse electric (TE) or transverse magnetic (TM) modes [19] can also propagate with different velocities within a practical cylindrical coax, interfering with each other producing distortion of the signal.

The frequency of operation for a specific outer conductor size is then limited by the highest usable cutoff frequency before undesirable modes of propagation occur.

In order to prevent higher order modes from being launched, the radiuses of the coaxial conductors must be reduced, diminishing the amount of power that can be transmitted.

On the other hand at high frequencies it is impossible to make the cylindrical coaxial line in the small size necessary to propagate the TEM mode alone.

The research described in this paper demonstrates the propagation on the fundamental TEM wave along the ideal MSCC.

Since the mode of transmission on an ideal line is the TEM wave, the relations for input impedance, reflection coefficient, return loss (RL), standing wave ratio (SWR), and so forth, given afterward in the next sections, are applicable in general to the spiral transmission lines (see [18] Chapter 3).

The metal double spiral coaxial cable or MDSCC, resulting from the superposition of two spiral conductors that share the same geometrical axis, can be made multi-turn. The amount of heat generated by the losses for heating can be distributed over a larger area and this would lower the temperature and raise the reliability of the line.

In fact, operation at higher temperatures results in a reduction in the life expectancy and reliability of the transmission line relative to the lower temperature performance.

Applications like nanoscale optical components for integration on semiconductor chips could benefit from these characteristics of the MSCC.

Where signal integrity is important, coaxial cables are needed to be shielded against radio frequency noise (RF noise). The multiturn MDSCC is naturally shielded because the highest part of the elm energy can be distributed on the inner part of the cable, which protects small signals from interference due to external electric fields.

A new class of spiral passive components, computer-aided engineering (CAE) tools as well as electromagnetic (EM) simulators, is required before new high-frequency spiral RF/microwave circuits will be implemented.

The spiral geometry occurs widely in nature; examples like the *spiral galaxies* are found at the universe level while the *myelin bundles* are common in the microcosm of the neuron cells.

Recently, a new spiral optical fibre has been proposed both in the fundamental mode [20] and in the higher order modes [21] operation.

Spirals are also of extreme interest to the field of the new metamaterials and invisible cloaking [22].

Myelinated nerve fibers are micro-spiral coaxial cables ($g \ll 1$) whose electric behaviour is still today described by neurophysiologists using *W. Thomson's* (later known as *Lord Kelvin*) *cable formula* [23] of the 1860s, which determines the velocity of the signal propagating in saltatory conduction [23, 24].

Cable theory in neurobiology has a long history, having first been applied to neurons in 1863 by *C. Matteucci* [25] who discovered that if a constant current flows through a portion of a platinum wire covered with a sheath saturated with fluid,

extra-polar current can be led off which corresponds to the electrotonic current of nerves.

Since the 1950s–60s myelinated nerves have been recognized to have a spiral structure and to behave like a high loss coaxial cable [26, 27] with negligible inductance.

The mathematical model presented in this paper can be used to refine the elm theory of the myelinated nerves by taking into account their spiral geometry.

In a coaxial guide, the determination of the electromagnetic fields within any region of the guide is dependent upon one's ability to explicitly solve the *Maxwell field equations* in an appropriate coordinate system [28].

Let us consider *Maxwell's equations*

$$\begin{gathered}\nabla \times \vec{E} = -j\omega\mu\vec{H},\\ \nabla \times \vec{H} = j\omega\epsilon\vec{E},\\ \nabla \cdot \vec{E} = 0,\\ \nabla \cdot \vec{H} = 0,\end{gathered} \tag{1}$$

where the time variation of the fields is assumed to be $\exp(j\omega t)$.

In view of the nature of the boundary surface, it is convenient to separate these field equations into components parallel and transverse to the waveguide z-axis.

This is achieved by scalar and vector multiplication of (1) with $\hat{e}_z$, a unit vector in the z direction, thus obtaining

$$\begin{gathered}\nabla_\perp \cdot \left(\hat{e}_z \times \vec{E}_\perp\right) = -j\omega\mu H_z,\\ \nabla_\perp \cdot \left(\hat{e}_z \times \vec{H}_\perp\right) = j\omega\epsilon E_z,\end{gathered} \tag{2}$$

$$\begin{gathered}\nabla_\perp E_z - \frac{\partial E_\perp}{\partial z} = -j\omega\mu\left(\hat{e}_z \times H_\perp\right),\\ \nabla_\perp H_z - \frac{\partial H_\perp}{\partial z} = j\omega\epsilon\left(\hat{e}_z \times E_\perp\right).\end{gathered} \tag{3}$$

Since the transmission line description of the electromagnetic field within uniform guides is independent of the particular form of the coordinate system employed to describe the cross section, no reference to cross-sectional coordinates is made on deriving the *telegrapher's equation* [28, 29].

Substituting (2) into (3) we obtain

$$\begin{gathered}\frac{\partial E_\perp}{\partial z} = -jk\xi\left(\vec{\epsilon} + \frac{1}{k^2}\nabla_\perp\nabla_\perp\right)\cdot\left(\vec{H}_\perp \times \hat{e}_z\right),\\ \frac{\partial H_\perp}{\partial z} = -jk\eta\left(\vec{\epsilon} + \frac{1}{k^2}\nabla_\perp\nabla_\perp\right)\cdot\left(\hat{e}_z \times \vec{E}_\perp\right).\end{gathered} \tag{4}$$

Vector notation is employed with the following meanings for the symbols:

$E_\perp = E_\perp(x, y, z)$ = the rms electric field intensity transverse to the z-axis.

$H_\perp = H_\perp(x, y, z)$ = the rms magnetic field intensity transverse to the z-axis.

η = intrinsic impedance of the medium $1/\eta = \sqrt{\mu/\epsilon}$.

$k = \omega\sqrt{\mu\epsilon} = 2\pi/\lambda$ = propagation constant in medium or the wavenumber (see [28] page 3).

$\nabla_\perp$ = gradient operator transverse to z-axis = $\nabla - \hat{e}_z(\partial/\partial z)$.

$\vec{\epsilon}$ = unit dyadic defined such that $\vec{\epsilon}\cdot\vec{A} = \vec{A}\cdot\vec{\epsilon} = \vec{A}$.

Equations (4) and (2), which are fully equivalent to the *Maxwell equations*, make evident the separate dependence of the field on the cross-sectional coordinates and on the longitudinal coordinate z. The cross-sectional dependence may be integrated out of (4) by means of a suitable set of vector orthogonal functions provided they satisfy appropriate conditions on the boundary curve or curves s of the cross section.

Such vector functions are known to be of two types: the *E-mode* functions e_i' defined by

$$\begin{gathered}e_i' = -\nabla_\perp\Phi_i,\\ h_i' = \hat{e}_z \times e_i',\end{gathered} \tag{5}$$

where

$$\begin{gathered}\nabla_\perp^2\Phi_i + k_{ci}'^2\Phi_i = 0,\\ \Phi_i = 0 \quad \text{on } s \quad \text{if } k_{ci}' \neq 0,\\ \frac{\partial\Phi_i}{\partial s} = 0 \quad \text{on } s \quad \text{if } k_{ci}' = 0,\end{gathered} \tag{6}$$

and the *H-mode* functions e_i'' defined by

$$\begin{gathered}e_i'' = \hat{e}_z \times \nabla_\perp\Psi_i,\\ h_i'' = \hat{e}_z \times e_i'',\end{gathered} \tag{7}$$

where

$$\begin{gathered}\nabla_\perp^2\Psi_i + k_{ci}''^2\Psi_i = 0,\\ \frac{\partial\Psi_i}{\partial n} = 0 \quad \text{on } s,\end{gathered} \tag{8}$$

where i denotes a double index and $\vec{n}$ is the outward normal to s in the cross-section plane.

The constants k_{ci}'' and k_{ci}' are defined as the cutoff wave numbers or eigenvalues associated with the guide cross section.

The functions e_i possess the vector orthogonality properties

$$\begin{gathered}\iint e_i' \cdot e_j' dS_\perp = \iint e_i'' \cdot e_j'' dS_\perp = \begin{cases}1 & \text{for } i = j\\ 0 & \text{for } i \neq j,\end{cases}\\ \iint e_i' \cdot e_j'' dS_\perp = 0,\end{gathered} \tag{9}$$

with the integration extended over the entire guide cross section with surface $S_\perp$.

The total average power flow along the guide in the z direction is

$$P_z = \frac{1}{2}\,\mathrm{Re}\left(\iint E_\perp \times H_\perp^* \cdot \hat{e}_z dS_\perp\right), \tag{10}$$

where all quantities are rms and the asterisk denotes the complex conjugate.

In TEM modes, both E_z and H_z vanish, and the fields are fully transverse. Their cutoff condition $k_c^2 = 0$ or $\omega = \beta c$ (where c is the speed of the light) is equivalent to the following relation [28]:

$$\vec{H}_\perp = \frac{1}{\eta}\hat{e}_z \times \vec{E}_\perp, \tag{11}$$

between the electric and magnetic transverse fields, where $\eta = \sqrt{\mu/\epsilon}$ is the medium impedance so that $\eta/c = \mu$ and $\eta c = 1/\epsilon$.

The electric field $\vec{E}_\perp$ is determined from the rest of *Maxwell's* equations which read

$$\begin{aligned} \nabla_\perp \times \vec{E}_\perp &= 0, \\ \nabla \cdot \vec{E}_\perp &= 0. \end{aligned} \tag{12}$$

These are recognized as the field equations of an equivalent two-dimensional electrostatic problem.

Once the electrostatic solution $\vec{E}_\perp$ is found, the magnetic field is constructed from (11).

Because of the relationship between $\vec{E}_\perp$ and $\vec{H}_\perp$, the Poynting vector S_z will be

$$S_z = \frac{1}{2}\,\mathrm{Re}\left(\vec{E}_\perp \times \vec{H}_\perp^*\right) \cdot \hat{e}_z = \frac{1}{\eta}\left|\vec{E}_\perp\right|^2 = \eta\left|\vec{H}_\perp\right|^2. \tag{13}$$

2. The Spiral Differential Geometry

For the MSCC structures it is difficult to construct solutions for *Laplace's equation* with polar or cartesian coordinates.

The conformal mapping technique is a powerful method for solving two-dimensional potential problems and mapping the boundaries into a simpler configuration for which solutions to *Laplace's equation* are easily found [17, 18].

For the specific purposes of the MSCC, the following spiral coordinates based on a generalization of the *Schwarz-Christoffel* mapping (see appendix) are introduced:

$$\begin{aligned} x &= e^{(\delta/g - g\theta)}\cos(\delta+\theta), \\ y &= e^{(\delta/g - g\theta)}\sin(\delta+\theta), \\ z &= z, \end{aligned} \tag{14}$$

where θ, δ represent the spiral coordinates and $g > 0$ is a constant which characterizes the transformation (see appendix).

As it can be seen in Figure 1, the equation $\delta = \text{const.}$ represented by a vertical line in the δ-θ plane corresponds to a logarithmic spiral into the x-y plane and a constant coordinate line of the spiral mapping.

Observing (14) it appears clear that for $g\theta - \delta^*/g \to 0$, where δ^* is a constant, the curve in the x-y plane locally reduces (for $|\theta| \ll 1$, $g \ll 1$) to an *Archimedean spiral*.

The region between the two coaxial spirals maps into the region inside the polygon bounded by the coordinate-lines $\theta = \theta_1, \theta = \theta_2$ and $\delta = \delta_1, \delta = \delta_2, \delta = \delta_1 - 2\pi g^2/(1+g^2)$ [18] (see Figure 1(b)).

It is also worth to observe that, if $\delta_2 - \delta_1 = 2q\pi g^2/(1+g^2)$, $q \in \mathbb{Z}$, the two spirals $\delta = \delta_1$, $\delta = \delta_2$ are identical apart from a shift of $\Delta\theta_s = 2q\pi/(1+g^2)$.

We then require $|\delta_2 - \delta_1| < 2\pi g^2/(1+g^2)$ in order to avoid cyclic spirals with $\delta > \delta_2$ in the middle of the two with $\delta = \delta_1$ and $\delta = \delta_2$.

The differential one form of the spiral transformation or dual basis results in

$$\begin{aligned} dx &= \frac{\partial x}{\partial \delta}d\delta + \frac{\partial x}{\partial \theta}d\theta + \frac{\partial x}{\partial z}dz, \\ dy &= \frac{\partial y}{\partial \delta}d\delta + \frac{\partial y}{\partial \theta}d\theta + \frac{\partial y}{\partial z}dz, \\ dz &= dz. \end{aligned} \tag{15}$$

The arc length $d\ell$ is given by

$$\begin{aligned} d\ell^2 &= dx^2 + dy^2 + dz^2 \\ &= g_{\delta\delta}d\delta^2 + g_{\theta\theta}d\theta^2 + g_{zz}dz^2, \end{aligned} \tag{16}$$

where

$$\begin{aligned} h_\delta^2 &= g_{\delta\delta} = e^{(2(\delta/g)-2g\theta)}\left(1 + \frac{1}{g^2}\right), \\ h_\theta^2 &= g_{\theta\theta} = e^{(2(\delta/g)-2g\theta)}\left(1 + g^2\right), \\ h_z^2 &= g_{zz} = 1, \qquad g_{\delta\theta} = g_{\delta z} = g_{\theta z} = 0 \end{aligned} \tag{17}$$

are the components of the *metric tensor* and *Lamè coefficients*.

The infinitesimal volume element is given by

$$dV = \|J\|\, d\delta\, d\theta\, dz = e^{(2(\delta/g)-2g\theta)}\frac{1+g^2}{g}d\delta\, d\theta\, dz, \tag{18}$$

where the J is the *Jacobian* of the spiral transformation.

Let us now define the spiral natural basis vectors $\bar{e}_\delta, \bar{e}_\theta, \bar{e}_z$:

$$\begin{aligned} \bar{e}_\delta &= \frac{\partial \vec{x}}{\partial \delta} \\ &= e^{(\delta/g - g\theta)}\left(\frac{1}{g}\cos(\delta+\theta) - \sin(\delta+\theta)\right)\bar{e}_x \\ &\quad + e^{(\delta/g - g\theta)}\left(\frac{1}{g}\sin(\delta+\theta) + \cos(\delta+\theta)\right)\bar{e}_y, \end{aligned}$$

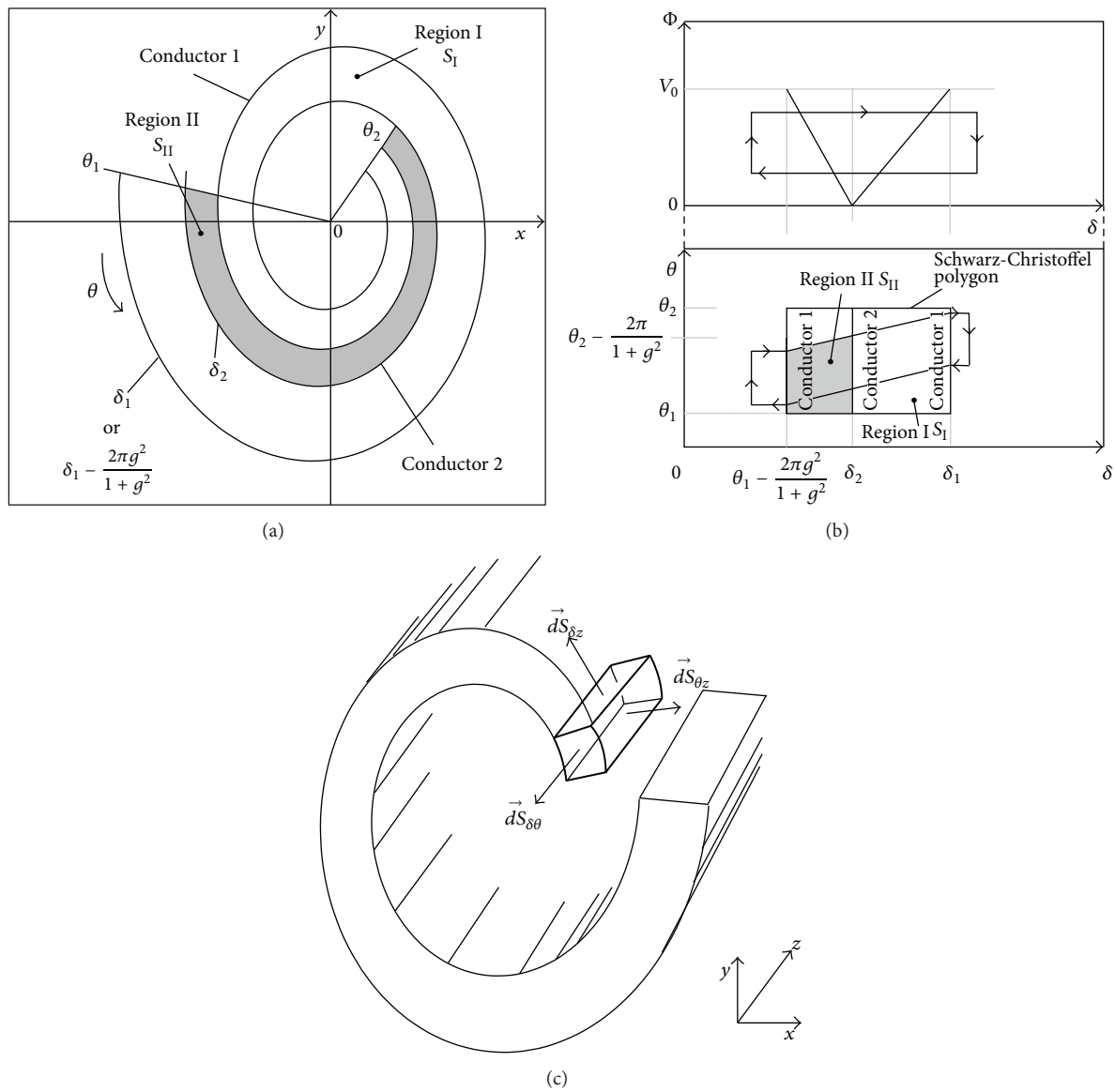

Figure 1: (a) The spiral coordinates lines. (b) The mapping of the spiral coaxial section and the scalar potential $\Phi(\delta, \theta)$, solution to the equivalent Laplace's equation. (c) The differential spiral surfaces.

$$\begin{aligned}\bar{e}_\theta &= \frac{\partial \vec{x}}{\partial \theta} \\ &= e^{(\delta/g - g\theta)}\left(-g\cos(\delta+\theta) - \sin(\delta+\theta)\right)\bar{e}_x \\ &\quad + e^{(\delta/g - g\theta)}\left(-g\sin(\delta+\theta) + \cos(\delta+\theta)\right)\bar{e}_y, \\ \bar{e}_z &= \frac{\partial \vec{x}}{\partial z} = \bar{e}_z\end{aligned} \tag{19}$$

in terms of the cartesian basis vectors $\bar{e}_x, \bar{e}_y, \bar{e}_z$.

The infinitesimal surface elements transverse and longitudinal along the z-axis (see Figure 1) are given by

$$\begin{aligned}\left\|d\vec{S}_{\delta\theta}\right\| &= dS_\perp = \left\|\frac{\partial \vec{x}}{\partial \delta} \times \frac{\partial \vec{x}}{\partial \theta}\right\| d\delta\, d\theta \\ &= e^{(2\delta/g - 2g\theta)}\left(\frac{1}{g} + g\right) d\delta\, d\theta, \\ \left\|d\vec{S}_{\theta z}\right\| &= \left\|\frac{\partial \vec{x}}{\partial \theta} \times \frac{\partial \vec{x}}{\partial z}\right\| d\theta\, dz = e^{(\delta/g - g\theta)}\sqrt{1+g^2}\, dz\, d\theta, \\ \left\|d\vec{S}_{\delta z}\right\| &= \left\|\frac{\partial \vec{x}}{\partial \delta} \times \frac{\partial \vec{x}}{\partial z}\right\| d\delta\, dz = e^{(\delta/g - g\theta)}\frac{\sqrt{1+g^2}}{g}\, dz\, d\delta.\end{aligned} \tag{20}$$

We then define the natural unitary spiral basis vectors

$$\hat{e}_\delta = \frac{\bar{e}_\delta}{h_\delta}, \qquad \hat{e}_\theta = \frac{\bar{e}_\theta}{h_\theta}, \qquad \hat{e}_z = \frac{\bar{e}_z}{h_z}. \tag{21}$$

The usual unitary relations of orthogonality hold; that is,

$$\hat{e}_\delta = \hat{e}_\theta \times \hat{e}_z, \qquad \hat{e}_\theta = \hat{e}_z \times \hat{e}_\delta, \qquad \hat{e}_z = \hat{e}_\delta \times \hat{e}_\theta,$$
$$\hat{e}_\delta \cdot \hat{e}_\theta = 0 = \hat{e}_\delta \cdot \hat{e}_z = \hat{e}_\theta \cdot \hat{e}_z = 0. \tag{22}$$

In Figure 1 a vertical segment in the θ-δ plane corresponds to a piece of spiral in the x-y plane; the circle is a particular spiral defined by the relation $\theta = \delta/g^2 - K/g$.

The radius vector in spiral coordinates becomes

$$\vec{r} = \frac{e^{(\delta/g - g\theta)}}{\sqrt{1+g^2}} \left(\hat{e}_\delta - g\hat{e}_\theta\right) + z\hat{e}_z. \tag{23}$$

Logarithmic spirals are analogous to the straight line. The orthogonal spiral is obtained, exactly as for the straight lines by replacing the g factor (which is analogous to the slope for the straight lines) with $g_\perp = -1/g$.

It is also possible to define the orthogonal spiral coordinate mapping as follows:

$$x = e^{(-g\delta + \theta/g)} \cos(\delta + \theta),$$
$$y = e^{(-g\delta + \theta/g)} \sin(\delta + \theta), \tag{24}$$
$$z = z.$$

3. The TEM Mode for the Spiral Waveguide

Let us consider two separate perfectly conducting spiral conductors with uniform cross section, infinitely long and oriented parallel to the z-axis; for such a structure a TEM mode of propagation is possible [18].

Laplace's equation of this line transformed by means of a spiral conformal mapping [17, 18], which is the generalization of the polar conformal mapping (see appendix), is

$$\frac{e^{-2(\delta/g)+2g\theta}}{1+g^2}\left[g^2\frac{\partial^2\Phi}{\partial\delta^2} + \frac{\partial^2\Phi}{\partial\theta^2}\right] = 0, \tag{25}$$

where the scalar electric potential $\Phi(\delta,\theta)$ represents the solution to the equivalent electrostatic problem of the transverse electromagnetic TEM mode propagating along the MSCC.

This equation has to be solved into two separate independent open regions I, II where the solution must be continuous with derivatives:

$$\Phi \in \mathscr{C}^{(0)}\left[\left[\delta_1 - \frac{2\pi g^2}{1+g^2}, \delta_2\right] \times (-\infty,\infty)\right]$$
$$\cap\, \mathscr{C}^{(2)}\left[\left[\delta_1 - \frac{2\pi g^2}{1+g^2}, \delta_2\right] \times (-\infty,\infty)\right], \tag{26}$$
$$\Phi \in \mathscr{C}^{(0)}\left[[\delta_2,\delta_1] \times (-\infty,\infty)\right]$$
$$\cap\, \mathscr{C}^{(2)}\left[[\delta_2,\delta_1] \times (-\infty,\infty)\right].$$

The derivative of the electric potential represents the electric and the magnetic fields whose values are not continuous at the two spiral metal boundary walls. In Figure 3(a) MDSCC partially composed of two infinite ideal spiral conductors filled with dielectric material having a permittivity $\epsilon = \epsilon_0\epsilon_r$ is shown. The MDSCC has much in common with the parallel plate line [17]; the two spiral conductors are considered infinitely wide ($\theta \in [-\infty,\infty]$) and separated by $\Delta\delta = 2\pi g^2/(1+g^2)$.

The potential $\Phi(\delta,\theta)$ is subject to the following boundary conditions in the region I (see Figure 1)

$$\Phi(\delta_1,\theta) = V_0,$$
$$\Phi(\delta_2,\theta) = 0 \quad \forall\theta \in (-\infty,\infty) \tag{27}$$

and in the region II

$$\Phi(\delta_2,\theta) = 0,$$
$$\Phi\left(\delta_1 - \frac{2\pi g^2}{1+g^2}, \theta\right) = V_0 \quad \forall\theta \in (-\infty,\infty). \tag{28}$$

V_0 must be the same in both cases of (27) and (28) because $\delta = \delta_1$ and $\delta = \delta_1 - 2\pi g^2/(1+g^2)$ correspond to the same conductor (see Figure 1(b); cyclic spiral) and the potential must be continuous at the spiral metal walls.

By the method of separation of variable, let $\Phi(\delta,\theta)$ be expressed in product form as

$$\Phi(\delta,\theta) = R(\delta)\,P(\theta). \tag{29}$$

Substituting (29) into (25) and dividing by RP give

$$\frac{g^2}{R(\delta)}\frac{\partial^2 R(\delta)}{\partial\delta^2} + \frac{1}{P(\theta)}\frac{\partial^2 P(\theta)}{\partial\theta^2} = 0. \tag{30}$$

The two terms in (30) must be equal to constants, so that

$$\frac{g^2}{R(\delta)}\frac{\partial^2 R(\delta)}{\partial\delta^2} = -k_\delta^2, \tag{31}$$

$$\frac{1}{P(\theta)}\frac{\partial^2 P(\theta)}{\partial\theta^2} = -k_\theta^2, \tag{32}$$

$$k_\delta^2 + k_\theta^2 = 0. \tag{33}$$

The general solution to (32) is

$$P(\theta) = A\cos(k_\theta\theta) + B\sin(k_\theta\theta). \tag{34}$$

Now, because the boundary conditions (27), (28) do not vary with θ, the potential $\Phi(\delta,\theta)$ should not vary with θ. Thus, k_θ must be zero. By (33), this implies that k_δ must also be zero, so that (31) for $R(\delta)$ reduces to

$$\frac{\partial^2 R(\delta)}{\partial\delta^2} = 0, \tag{35}$$

and so

$$\Phi(\delta,\theta) = C\delta + D. \tag{36}$$

The equivalent electrostatic problem in the plane (δ, θ) is the problem of finding the potential distribution between two plates [18].

Applying the boundary conditions of (27) to (36) gives two equations for the constants C and D in the region I:

$$\begin{aligned} \Phi(\delta_1, \theta) &= 0 = C_{\mathrm{I}}\delta_1 + D_{\mathrm{I}}, \\ \Phi(\delta_2, \theta) &= V_0 = C_{\mathrm{I}}\delta_2 + D_{\mathrm{I}}. \end{aligned} \tag{37}$$

At the same time the boundary conditions of (28) into (36) give two equations for the constants C and D in the region II:

$$\begin{aligned} \Phi(\delta_2, \theta) &= V_0 = C_{\mathrm{II}}\delta_2 + D_{\mathrm{II}}, \\ \Phi\left(\delta_1 - \frac{2\pi g^2}{1+g^2}, \theta\right) &= 0 = C_{\mathrm{II}}\left(\delta_1 - \frac{2\pi g^2}{1+g^2}\right) + D_{\mathrm{II}}. \end{aligned} \tag{38}$$

After solving for $C_{\mathrm{I,II}}$ and $D_{\mathrm{I,II}}$, we can write the final solution for $\Phi(\delta, \theta)$:

$$\begin{aligned} &\Phi(\delta, \theta) = \frac{V_0}{\delta_2 - \delta_1}(\delta - \delta_1) \\ &\text{region I } \theta \in [-\infty, \infty], \quad \delta \in [\delta_2, \delta_1], \\ &\Phi(\delta, \theta) = \frac{V_0}{\delta_2 - \delta_1 + 2\pi g^2/(1+g^2)}\left(\delta - \delta_1 + \frac{2\pi g^2}{1+g^2}\right) \\ &\text{region II } \theta \in [-\infty, \infty], \quad \delta \in \left[\delta_1 - \frac{2\pi g^2}{1+g^2}, \delta_2\right]. \end{aligned} \tag{39}$$

The $\vec{E}$ and $\vec{H}$ fields can now be found using (5) and (39):

$$\text{region I} \begin{cases} \vec{E}_\perp = E_\delta \hat{e}_\delta = -\nabla_\perp \Phi = -\dfrac{e^{(-\delta/g+g\theta)}}{\sqrt{1+g^2}} \dfrac{gV_0}{\delta_2 - \delta_1}\hat{e}_\delta, \\ E_\theta = 0, \\ \vec{H}_\perp = H_\theta \hat{e}_\theta = \dfrac{1}{\eta}\hat{e}_z \times E_\delta \hat{e}_\delta \\ \quad = \dfrac{ge^{(-\delta/g+g\theta)}}{\eta\sqrt{1+g^2}} \dfrac{V_0}{\delta_2 - \delta_1}\hat{e}_\theta, \\ H_\delta = 0. \end{cases}$$

$$\text{region II} \begin{cases} \vec{E}_\perp = E_\delta \hat{e}_\delta = -\nabla_\perp \Phi \\ \quad = -\dfrac{ge^{(-\delta/g+g\theta)}}{\sqrt{1+g^2}} \dfrac{V_0}{\delta_2 - \delta_1 + 2\pi g^2/(1+g^2)}\hat{e}_\delta, \\ E_\theta = 0, \\ \vec{H}_\perp = H_\theta \hat{e}_\theta = \dfrac{1}{\eta}\hat{e}_z \times E_\delta \hat{e}_\delta \\ \quad = \dfrac{ge^{(-\delta/g+g\theta)}}{\eta\sqrt{1+g^2}} \dfrac{V_0}{\delta_2 - \delta_1 + 2\pi g^2/(1+g^2)}\hat{e}_\theta, \\ H_\delta = 0. \end{cases} \tag{40}$$

While the electric and the magnetic fields together with the surface charge and current densities vary exponentially with the spiral coordinates (δ, θ), the potential remains constant on the two conductors.

The field distribution for the TEM mode in the MSCC depicted in Figure 2 is obtained by using (40) and the quiver-MATLAB function.

As stated by the *Gauss law* [30] the whole surface density σ of charge on each of the two spiral conductors, due to the discontinuity of the electric field, is

$$\sigma(\theta) = \epsilon \vec{E}_{\mathrm{II}} \cdot \vec{n} - \epsilon \vec{E}_{\mathrm{I}} \cdot \vec{n}, \tag{41}$$

where $\vec{n} \equiv \hat{e}_\delta$ is the normal to the spiral surface of the conductors whilst $\vec{E}_{\mathrm{I}}$ and $\vec{E}_{\mathrm{II}}$ are the electric fields seen from the regions I and II, respectively.

According to (41) the electric charge distribution follows the exponential electric field.

The two spiral metal conductors are in a parallel configuration; they have the same potential difference but two different capacities and two different surface charge distributions.

At the same time the total displacement current [30] due to the discontinuity of the magnetic fields at the two conductors is

$$\vec{J}_{S_{\mathrm{tot}}} = \vec{n} \times \vec{H}_{\mathrm{I}} - \vec{n} \times \vec{H}_{\mathrm{II}}. \tag{42}$$

The time-average stored electric energy per unit length [2, 17] in the MDSCC (see Figure 3) is

$$W_e = \frac{1}{2}\int_{S_\perp} \epsilon' \vec{E} \cdot \vec{E}^* dS_\perp, \tag{43}$$

while circuit theory gives $W_e = C'|V_0|^2/4$, resulting in the following expression for the capacitance per unit length:

$$C' = \frac{\epsilon'}{|V_0|^2}\int S_\perp \vec{E} \cdot \vec{E}^* dS_\perp, \quad [\mathrm{F/m}]. \tag{44}$$

As in the case of the parallel plate waveguide, the MSCC is composed of finite strips.

The electric field lines at the edge of the finite spiral conductors are not perfect spirals, and the field is not entirely contained between the conductors.

The azimuthal length in real multiturn MDSCC is assumed to be much greater than the separation between the conductors ($|\theta_1 - \theta_2| \gg \Delta\delta$) with $|\theta_1|$, $|\theta_2|$ not too high as in the case of the myelin bundles, so that the fringing fields can be ignored [2].

Furthermore, the minimum distance between the two spiral conducting strips is chosen in such a way to avoid the dielectric voltage breakdown.

Although the MDSCC line is modeled with two capacitors, it is composed by two and not three conductors as it would be in the case of the parallel plates.

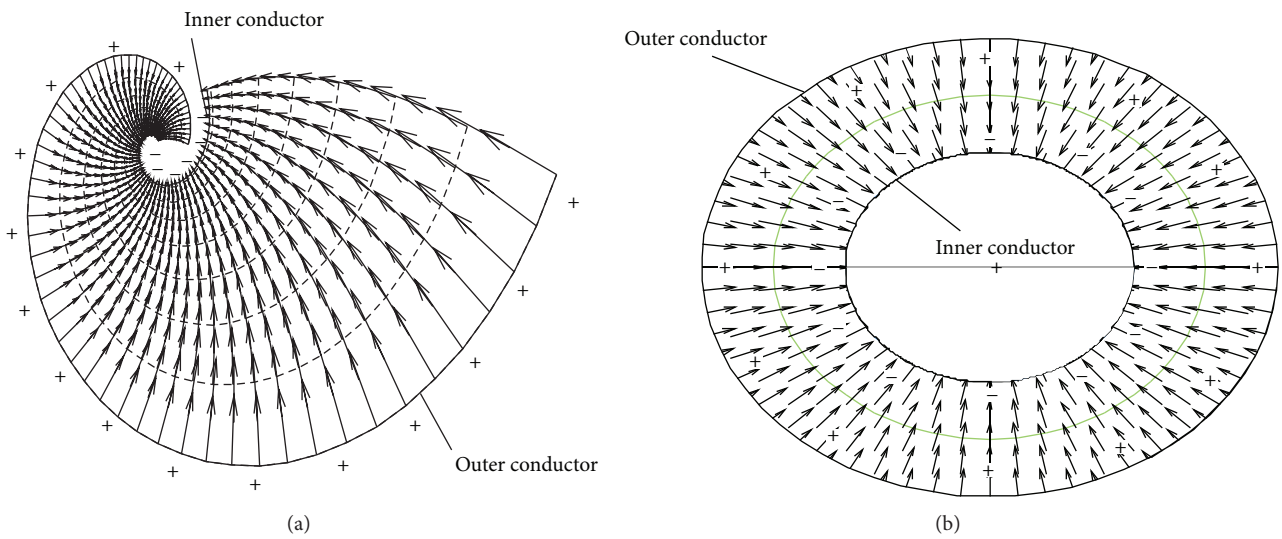

Figure 2: Field distribution for the TEM mode in the (a) MSCC, (b) cylindrical coax, obtained using the quiver-MATLAB function (simulations on Pentium 4, 3.2 Ghz, average CPU time: 4 min).

The two capacitors are different because their spiral dimensions are different; consequently the two capacitances are determined by

$$C_1' = \frac{\epsilon'}{|V_0|^2}\int_{S_{\mathrm{I}}} \vec{E}_{\mathrm{I}} \cdot \vec{E}_{\mathrm{I}}^* dS_\perp = \frac{g\epsilon'(\theta_2-\theta_1)}{\delta_1-\delta_2},$$
$$C_2' = \frac{\epsilon'}{|V_0|^2}\int_{S_{\mathrm{II}}} \vec{E}_{\mathrm{II}} \cdot \vec{E}_{\mathrm{II}}^* dS_\perp \tag{45}$$
$$= \frac{g\epsilon'\left(\theta_2-\theta_1-2\pi/\left(1+g^2\right)\right)}{\left(\delta_2-\delta_1+2\pi g^2/\left(1+g^2\right)\right)}, \quad \theta_2 > \theta_1.$$

Thus,

$$C_{\mathrm{tot}}' = C_1' + C_2' = \epsilon g W\left(\frac{\theta_2-\theta_1}{\delta_1-\delta_2} + \frac{\theta_2-\theta_1-2\pi/\left(1+g^2\right)}{\delta_2-\delta_1+2\pi g^2/\left(1+g^2\right)}\right). \tag{46}$$

This value represents the capacitance $C_{\mathrm{tot}}' = C_{\mathrm{tot}}/W$ (e.g., farads/meter) per unit length of the spiral coaxial line with finite azimuthal dimension $\theta_1 - \theta_2$ for the first greater capacitor and $\theta_2 - \theta_1 - 2\pi/(1+g^2)$ for the smaller one (see Figure 1).

If the number of spiral turns become high enough, the difference in terms of θ between the two capacitors will be negligible.

In order to determine the inductance L' per unit length of the MDSCC, we observe that the magnetic field is orthogonal to the electric field.

The magnetic fluxes over the two infinitesimal areas $dS_{\mathrm{I}_{z\delta}}$ and $dS_{\mathrm{II}_{z\delta}}$ are (see Figure 4) $d\Phi_{\mathrm{I,II}} = \vec{B}_{\mathrm{I,II}_\perp} \cdot d\vec{S}_{\mathrm{I,II}_{z\delta}}$, while the total fluxes over the two spiral areas S_{I}, S_{II}, according to (40), are

$$\Phi_{\mathrm{I}} = \Phi_{\mathrm{II}} = WV_0\frac{\mu}{\eta}. \tag{47}$$

The fluxes per unit length are given by

$$\Phi_{\mathrm{I,II}}' = \frac{\Phi_{\mathrm{I,II}}}{W} = L' I_0. \tag{48}$$

Consequently

$$L' = Z_0\frac{\mu}{\eta}, \tag{49}$$

where Z_0 and I_0 are the impedances and current of the line, respectively.

As it can be noted from (48) there is only one current I_0 flowing along the spiral coaxial cable.

The time-average stored magnetic energy for unit length (at low frequencies for nondispersive media) of the MDSCC can be written as [2, 17]

$$W_m = \frac{\mu}{2}\int_{S_\perp} \vec{H} \cdot \vec{H}^* dS_\perp. \tag{50}$$

Circuit theory gives $W_m = LI_0^2/4$ in terms of the unique current of the line I_0 and results from the sum of two contributions $W_m = W_1 + W_2$.

Thus,

$$L' = \frac{\mu Z_0^2}{V_0^2}\left(\int_{S_{\mathrm{I}}} \vec{H} \cdot \vec{H}^* dS_\perp + \int_{S_{\mathrm{II}}} \vec{H} \cdot \vec{H}^* dS_\perp\right). \tag{51}$$

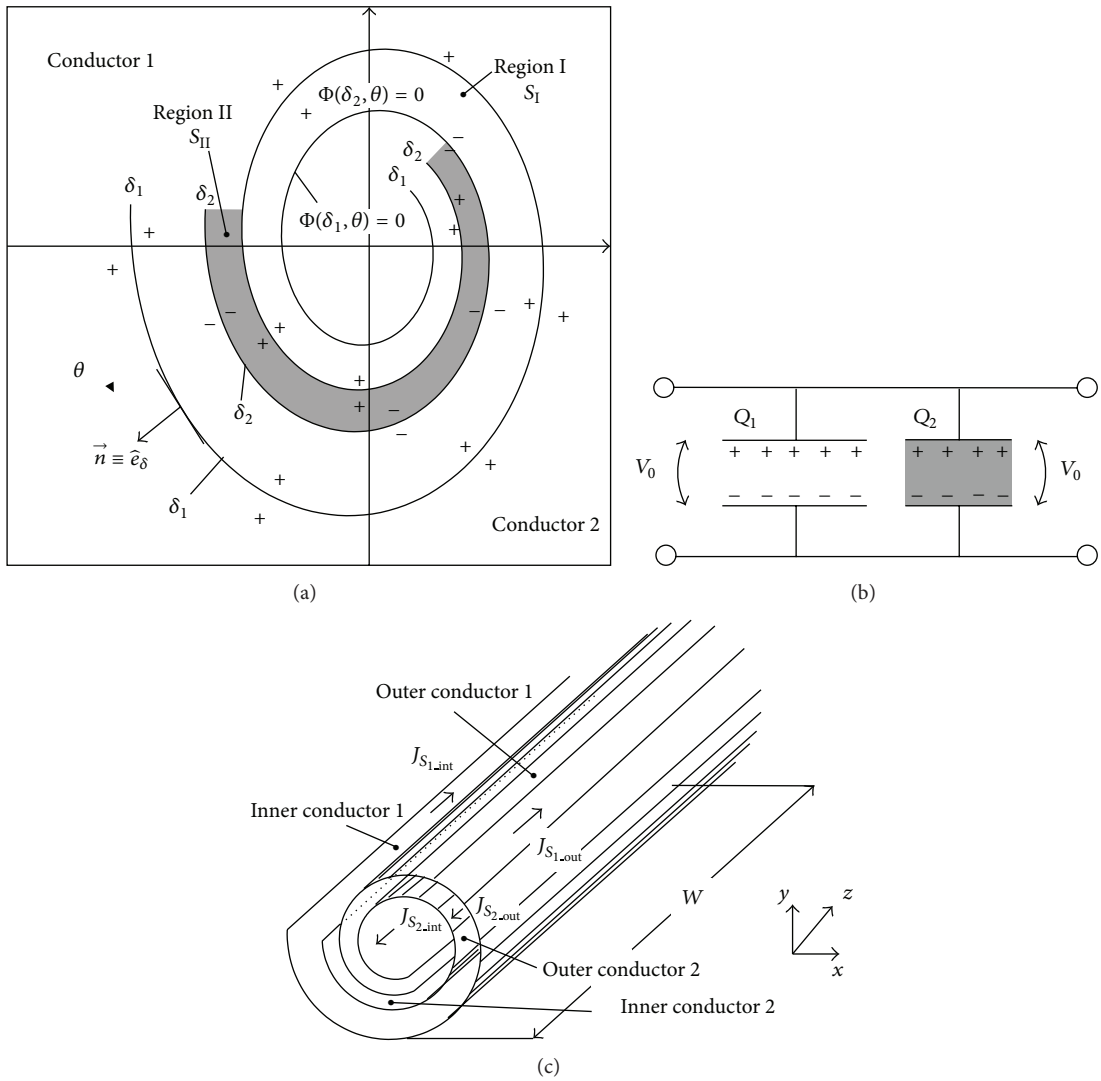

Figure 3: (a) Charge distributions in the electrostatic MDSCC section. (b) Parallel capacitors scheme of the electrostatic MDSCC. (c) Current distributions in the MDSCC.

Substituting (40) into (51), by considering the superposition of the two lines and using (49), gives

$$L' = \frac{\mu}{g} \cdot \left(\frac{\theta_2 - \theta_1}{\delta_1 - \delta_2} + \frac{\theta_2 - \theta_1 - 2\pi/\left(1 + g^2\right)}{\delta_2 - \delta_1 + 2\pi g^2/\left(1 + g^2\right)} \right)^{-1},$$
$$Z_0 = \frac{\eta}{g} \cdot \left(\frac{\theta_2 - \theta_1}{\delta_1 - \delta_2} + \frac{\theta_2 - \theta_1 - 2\pi/(1 + g^2)}{\delta_2 - \delta_1 + 2\pi g^2/(1 + g^2)} \right)^{-1}. \quad (52)$$

According to the classical electromagnetism (see, e.g., [16] page 563), a periodic wave incident upon a material body gives rise to a forced oscillation of free and bound charges synchronous with the applied field, producing a secondary field both inside and outside the body; the transmitted and reflected waves have the chance to excite propagating eigenmodes solutions to *Maxwell's* equations.

From the physical point of view, the light that passes through the entrance of the spiral waveguide is subject to multiple reflections. The historical work of Mie [31, 32] for the case of the spherical topology will be the reference starting point for the analysis of the light that passes through the open MSCC section and it is scattered by the spiral surface.

Localized surface plasmon polaritons (LSPP) [15] existing on a good metal surface can be excited, propagated, and scattered on the spiral lines. The enhancement of the electromagnetic field at the metal dielectric spiral interface could be responsible for surface-enhanced optical phenomena such as Raman scattering, fluorescence, and second harmonic generation (SHG) [33].

Nevertheless, the continuity of the tangential components of the magnetic and electric fields on each spiral

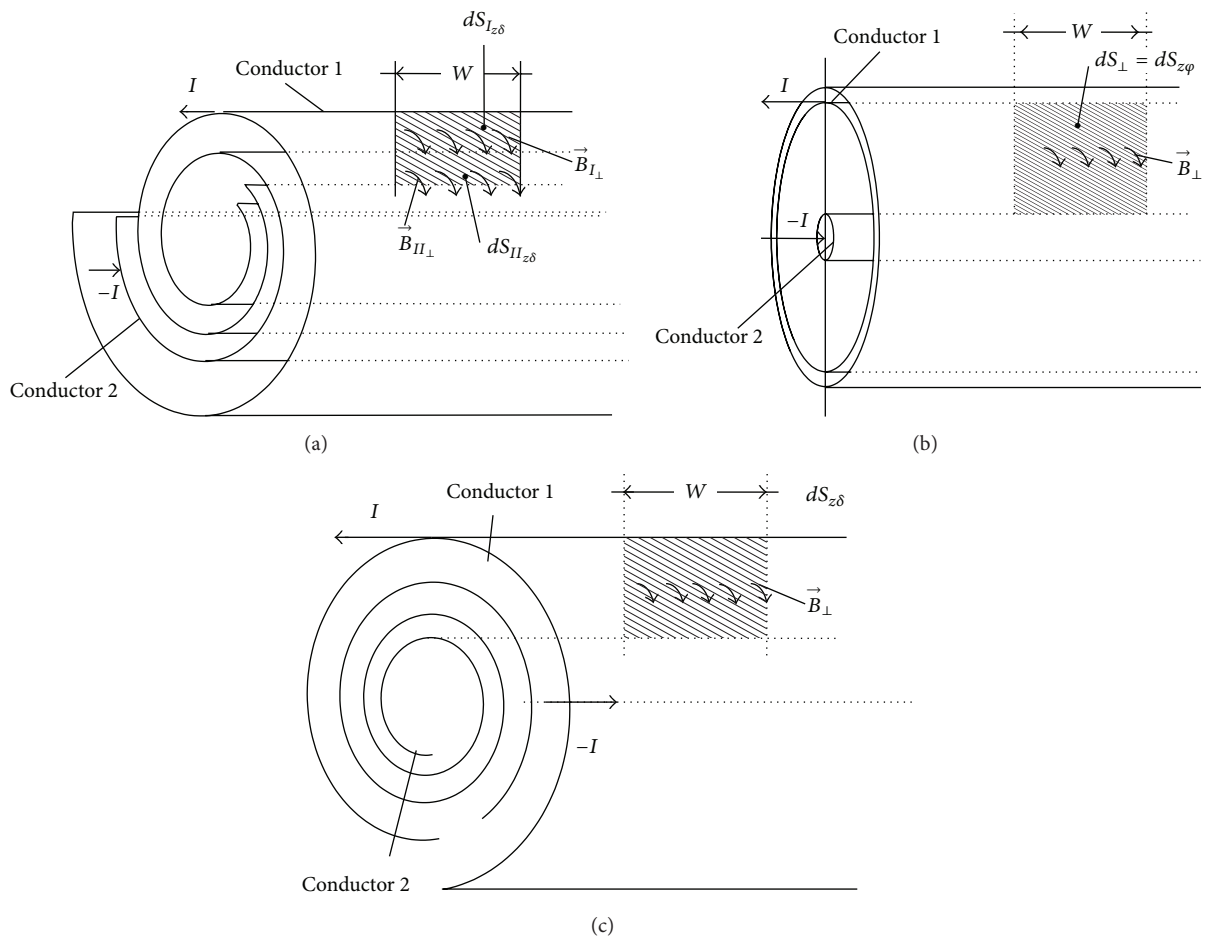

Figure 4: Surfaces for calculation of external inductances of (a) MDSCC, (b) cylindrical coaxial line [4], and (c) MSSCC.

metal-dielectric interface, which is essential in order to propagate the polaritons along the line [15] and includes the specific frequency-dependent dielectric constant of metals (real and imaginary parts), needs specific simulation methods [11] and dedicated mathematical analysis.

All these electromagnetic effects, which require advanced numerical techniques, validations, and comparisons in terms of CPU time, involve all the modes that pass through the waveguide. In spite of the interesting results and applications that these analyses could bring to the future of the spiral coaxial cables, their study is beyond the scope of this paper.

4. The Spiral Transmission Line

A transmission line consists of two or more conductors [2, 4, 17]. In this paper we consider two types of spiral transmission lines; their elements of line of infinitesimal length dz depicted in Figure 5 can be modeled as lumped-element circuits.

Although the MDSCC line is modeled with two capacitors, it is composed by two conductors with only one real capacitor. The series resistance R' per unit length represents the resistance due to the finite conductivity of the individual conductors, and the shunt conductance G' per unit length is due to dielectric loss in the material between the conductors.

For lossless lines, the three quantities Z, L', and C' are related as follows:

$$L' = \mu \frac{Z}{\eta}, \qquad C' = \epsilon \frac{\eta}{Z}, \tag{53}$$

where $\eta = \sqrt{\mu/\epsilon}$ is the characteristic impedance of the dielectric medium between the conductors.

The equations of the ideal spiral transmission line [4] depicted in Figure 5 are

$$\frac{\partial V}{\partial z} = -L' \frac{\partial I}{\partial t} - R' I, \qquad \frac{\partial I}{\partial z} = -C' \frac{\partial V}{\partial t} - G' V, \tag{54}$$

where R' is the resistance per unit length of the line, expressed in [Ω/m], and G' is the conductance per unit length of the line, measured in [S/m].

The two equations (54) for $R' = 0$ and $G' = 0$ can be combined to form *D'Alambert's wave equation* for either

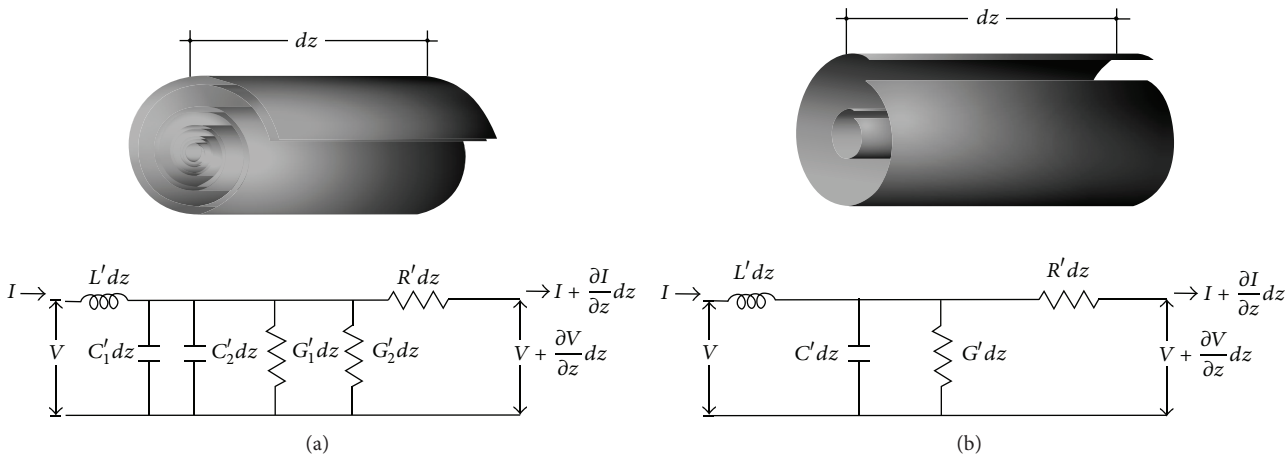

Figure 5: Element dz (a) MDSCC, (b) MSSCC, and their lumped-element equivalent circuits obtained using M-file with camlight programming tools (run on Pentium 4, 3.2 Ghz, average CPU time: 8 min).

variables [2], whose solutions are waves propagating along the ideal line with speed v:

$$\frac{\partial^2 V}{\partial z^2} = \frac{1}{v}\frac{\partial^2 V}{\partial t^2}, \qquad \frac{\partial^2 I}{\partial z^2} = \frac{1}{v}\frac{\partial^2 I}{\partial t^2}, \quad v = \frac{1}{\sqrt{L'C'}}. \tag{55}$$

Using the Fourier transform of the signals V, I

$$V(\omega) = \frac{1}{2\pi}\int_{-\infty}^{\infty} V(t)\, e^{-i\omega t} dt, \qquad I(\omega) = \frac{1}{2\pi}\int_{-\infty}^{\infty} I(t)\, e^{-i\omega t} dt. \tag{56}$$

The solution to (55) may be written in terms of exponentials

$$V = V_+ e^{-\gamma z} + V_- e^{\gamma z}, \qquad I = \frac{1}{Z_0}\left(V_+ e^{-\gamma z} - V_- e^{\gamma z}\right), \qquad \gamma^2 = -\omega^2 L'C'. \tag{57}$$

If a sinusoidal voltage is supplied to MDSCC with load impedance Z_L at $z = 0$, the reflection Γ and transmission τ coefficients will be

$$\Gamma = \frac{V_-}{V_+} = \frac{Z_L - Z_0}{Z_L + Z_0}, \qquad \tau = \frac{V_L}{V_+} = \frac{2Z_L}{Z_L + Z_0}. \tag{58}$$

If the terminating impedance is exactly equal to the characteristic impedance of the line there is no reflected wave; the line is matched with the load. According to (49) the reflected and the transmitted waves of a spiral coaxial line depend on the number of turns $n = \mathrm{Int}(\Delta\theta/2\pi)$, on the shift $\Delta\delta$ between the spiral walls, and on the spiral g factor.

5. Waves in a Lossy Spiral Coaxial Transmission Line

Conductors used in transmission lines have finite conductivity and exhibit series resistance R which increases with an increase in the frequency of operation [17] because of the skin effect. Furthermore the two conductors are separated by a dielectric medium which have a small amount of dielectric loss due to the polarization; consequently a small shunt conductance G is added to the circuit. Differentiating the lossy transmission equation (54) we obtain

$$\frac{\partial^2 V}{\partial z^2} = R'\left(G'V + C'\frac{\partial V}{\partial t}\right) + L'\left(C'\frac{\partial V}{\partial t} + C'\frac{\partial^2 V}{\partial t^2}\right), \qquad \frac{\partial^2 I}{\partial z^2} = R'\left(G'I + C'\frac{\partial I}{\partial t}\right) + L'\left(C'\frac{\partial I}{\partial t} + C'\frac{\partial^2 I}{\partial t^2}\right). \tag{59}$$

By using the Fourier transform of the signals V, I we obtain

$$\gamma = \left[-\omega^2 L'C' + R'G' + i\omega\left(R'C' + L'G'\right)\right]^{1/2}, \qquad Z_0 = \left(\frac{R' + i\omega L'}{G' + i\omega L'}\right)^{1/2}. \tag{60}$$

For most transmission lines the losses are very small; that is, $R' \ll \omega L'$ and $G' \ll \omega C'$; a binomial expansion of γ then holds:

$$\gamma \simeq i\omega\sqrt{L'C'} + \frac{1}{2}\sqrt{L'C'}\left(\frac{R'}{L'} + \frac{G'}{C'}\right) = \alpha + i\beta. \tag{61}$$

Thus the phase constant β remains unchanged with respect to the ideal line.

The expressions of R' reported in Table 2 can be found from the expression of the power loss per unit length due to the finite conductivity of the two metallic spiral conductors [2]; that is,

$$P_c = \frac{R_S}{2}\int_{S_{\theta z}} \vec{J}_S \cdot \vec{J}_S^{*}\, dS_{\theta z}, \tag{62}$$

where the argument of the integral is the scalar product of the displacement currents [30] flowing along the surfaces of the conductors.

In (62), $R_s = 1/(\sigma\delta_S)$ is the surface resistance of the conductors, where the skin depth, or characteristic depth of penetration, is defined as $\delta_S = \sqrt{2/(\omega\mu\sigma)}$.

The material filling the space between the conductors is assumed to have a complex permittivity $\epsilon = \epsilon' - i\epsilon''$, a permeability $\mu = \mu_0\mu_r$, and a *loss tangent* $\tan(\delta_{\text{mat}}) = \epsilon''/\epsilon'$.

The shunt conductance per unit length G' reported in Table 2 can be inferred from the time-average power dissipated per unit length in a lossy dielectric; that is,

$$P_d = \frac{\omega\epsilon''}{2}\int_{S_{\text{I}_\perp}} \vec{E}\cdot\vec{E}^* dS_\perp + \frac{\omega\epsilon''}{2}\int_{S_{\text{II}_\perp}} \vec{E}\cdot\vec{E}^* dS_\perp. \quad (63)$$

The total voltage and current waves on the line can then be written as a superposition of an incident and a reflected wave

$$V = V_+\left(e^{-\gamma z} + \Gamma e^{\gamma z}\right),$$
$$I = \frac{V_+}{Z_0}\left(e^{-\gamma z} - \Gamma e^{\gamma z}\right). \quad (64)$$

The time-average power flow along the line at the point z is

$$P_{\text{avg}} = \frac{1}{2}\frac{\left|V_{0_+}\right|^2}{Z_0}\left(1 - |\Gamma|^2\right). \quad (65)$$

When the load is mismatched, not all of the available power from the generator is delivered to the load, the presence of a reflected wave leads to standing waves [2], and the magnitude of the voltage on the line is not constant.

The return loss (RL) is

$$\text{RL} = -20\log|\Gamma| \quad [\text{dB}]. \quad (66)$$

A measure of the mismatch of a line is the standing wave ratio (SWR)

$$\text{SWR} = \frac{1 + |\Gamma|}{1 - |\Gamma|}. \quad (67)$$

At a distance $z = -l$ from the load, the input impedance seen looking toward the load is

$$Z_{\text{in}} = Z_0\frac{Z_L + iZ_0\tan\gamma l}{Z_L - iZ_0\tan\gamma l}. \quad (68)$$

The power delivered to the input of the terminated line at $z = -l$ is

$$P_{\text{in}} = \frac{1}{2}\frac{\left|V_{0_+}\right|^2}{Z_0}\left(e^{2\alpha l} - |\Gamma|^2 e^{2\alpha l}\right). \quad (69)$$

The difference $P_{\text{avg}} - P_{\text{in}}$ corresponds to the power lost in the line [2].

From (58) and (49) it appears clear that $|\Gamma|$, P_{avg}, RL, SWR, Z_{in}, and the power lost depend critically on the spiral factors of the line.

Particularly it is worth to point out that the g factor acts as a "control knob" of the electromagnetic propagation along the MDSCC.

6. Single Spiral Coaxial Cable and the Myelinated Nerves

The difficulty of using a single spiral surface to construct a coaxial line is due to the constraint of having the constant potential on the conductor.

The problem can be solved by using two independent stripes of the same single spiral surface with $|\theta_f - \theta_i| \le 2\pi$ and $|\theta_1|, |\theta_2|$ not too high, separated by a shift $\Delta\delta = 2n\pi g^2/(1+g^2)$ to form a system of two independent faced conductors with one grounded (as depicted in Figures 5(b) and 6(a)).

The metal single spiral coaxial cable (MSSCC) does not differ geometrically too much from the cylindrical coaxial design, especially for $g \ll 1$, but the first is an open framework whilst the second is a closed one.

Again, according to the conformal mapping theory [18], the equivalent electrostatic problem for the MSSCC in the plane (δ, θ) is just the problem of finding the potential distribution between two finite coordinate-plates like in the cylindrical case [18].

The potential $\Phi(\delta, \theta)$ for the TEM wave is now subject to the following boundary conditions:

$$\Phi(\delta_1, \theta) = 0 = C_m\delta_1 + D_m,$$
$$\Phi\left(\delta_1 + \frac{2n\pi g^2}{1+g^2}, \theta\right) = V_0 = C_m\left(\delta_1 + \frac{2n\pi g^2}{1+g^2}\right) + D_m, \quad (70)$$
$$\forall\theta \in \left[\theta_i, \theta_f\right], \quad \left|\theta_i - \theta_f\right| \le 2\pi.$$

Consequently the solution in (36) to *Laplace's* electrostatic equation (25) takes the form

$$\Phi(\delta, \theta) = V_0\frac{1+g^2}{2n\pi g^2}(\delta - \delta_1). \quad (71)$$

The electric and magnetic field for the MSSCC is simplified compared to the MDSCC; that is,

$$\vec{E}_\perp = E_\delta\hat{e}_\delta = -\nabla_\perp\Phi = \frac{e^{(-\delta/g+g\theta)}}{\sqrt{1+g^2}}\frac{gV_0\left(1+g^2\right)}{2n\pi g^2}\hat{e}_\delta,$$
$$E_\theta = 0,$$
$$\vec{H}_\perp = H_\theta\hat{e}_\theta = \frac{1}{\eta}\hat{e}_z \times E_\delta\hat{e}_\delta = -\frac{e^{(-\delta/g+g\theta)}}{\eta\sqrt{1+g^2}}\frac{V_0\left(1+g^2\right)}{2n\pi g}\hat{e}_\theta,$$
$$H_\delta = 0,$$
$$\forall\theta \in \left[\theta_{i_1}, \theta_{f_2}\right], \quad \delta \in \left[\delta_1, \delta_1 + \frac{2n\pi g^2}{1+g^2}\right]. \quad (72)$$

The total charge Q on the inner/outer conductors of MSSCC of length W is

$$Q = \int_{S_m}\sigma dS_{\theta z} = W\epsilon\frac{V_0\left(1+g^2\right)}{ng}. \quad (73)$$

Table 1: Values of capacitance for an average human myelinated nerve obtained with the SSCC and the cylindrical coax models.

Fibre diameter $[D]$	Axon diameter $[d]$	g_{mye}	ϵ_{mye}	Number of lamellae n_l	Core-conductor capacitance C_{mye} [34]	Single-coax capacitance C_{mye}	Cole's inductance L_{mye} [36]	Single-coax inductance L_{mye}
$\simeq 2\,\mu$m	$\simeq 1.4\,\mu$m	$\simeq 0.0009$	$\simeq 13$	$\simeq 16$	$\epsilon_0\epsilon_{\text{mye}}\dfrac{2\pi}{\log(D/d)}$ $\simeq 4.6\dfrac{nF}{m}$	$\epsilon_0\epsilon_{\text{mye}}\dfrac{1+g_{\text{mye}}^2}{2n_l g_{\text{mye}}}$ $\simeq 4\dfrac{nF}{m}$	$\dfrac{\mu_{\text{mye}}}{2\pi}\log(D/d)$ $\simeq 30\dfrac{nHenry}{m}$	$\mu_{\text{mye}} n_l \dfrac{g_{\text{mye}}}{1+g_{\text{mye}}^2}$ $\simeq 20\dfrac{nHenry}{m}$

Since the potential difference between the two conductors is $\Delta V = V_0$, the capacitance per unit length of the MSSCC with n turns between the two spiral conductors takes the following simplified form:

$$C' = \epsilon\frac{1+g^2}{ng}. \tag{74}$$

The myelin sheath in the "core-conductor" model is an electrically insulating phospholipid multilamellar spiral membrane surrounding the conducting axons of many neurons; it consists of units of double bilayers separated by 3 to 4 nm thick aqueous layers composed of 75–80% lipid and 20–25% protein. The two conductors in myelinated fibres coincide with the inner conducting axon and the outer conducting extracellular fluid (see Figure 6(b)).

The myelin sheath acts as an electrical insulator, forming a capacitor surrounding the axon, which allows for faster and more efficient conduction of nerve impulses than unmyelinated nerves.

In Table 1, a comparison between the SSCC and the core conductor models [34] of an average human myelinated nerve is proposed.

The diameter of the myelinated nerve fibre [35] grows according to the formula

$$D = d + 2\times n_l \times k_l, \tag{75}$$

where n_l is the number of lamellae bilayers, k_l is their average width, d is the diameter of the axon, and D is the diameter of the fibre.

Now, using the formula of the spiral mapping we have

$$\begin{aligned} d &= 2e^{\delta_m/g_m - g_m\theta_{i_1}}, \\ D &= 2e^{\delta_m/g_m - g_m\theta_{f_2}}, \end{aligned} \tag{76}$$

where θ_{i_1,f_2} are the initial and final angles of the myelin sheaths, and δ_m determine the lipid membrane spiral contour.

For $g_m \ll 1$ as in the case of the myelin, the thickness of the nth bilayer is nearly constant and the radius at which it occurs is $r_n = e^{\delta_m/g - 4n\pi g}$.

By taking as value of the thickness $k_l \simeq r_1 - r_0 = r_0(1 - e^{-4g_m\pi}) \simeq 0.018\,\mu$m [35] we have

$$g_{\text{mye}} \simeq \frac{1}{4\pi}\ln\left(\frac{d}{d-2k_l}\right). \tag{77}$$

According to the statistics [35], the nerve fiber diameter D is linearly related to the axon d diameter; that is, $D = C_0 + C_1 d$.

By taking $4\pi n_l = \theta_{i_1} - \theta_{f_2}$ (each lipid bilayer consists of two spiral turns $\theta_{i_1} \gg \theta_{f_2}$) and using (76), we have the following relation between the number of myelin lamellae n_l and the diameter d of the axon:

$$n_l(d) = \text{Int}\left\{\frac{1}{4\pi g_m}\log\left[\frac{C_0 + C_1 d}{d}\right]\right\} \tag{78}$$

which is confirmed by the statistics [35].

In the case of the SCC we have

$$\begin{aligned} L' &= \mu n\frac{g}{1+g^2}, \\ Z_0 &= \eta n\frac{g}{1+g^2}, \end{aligned} \tag{79}$$

where n represents the number of spiral turns between the outer spiral conductor and the inner one.

The transmitted power in SCC depends inversely on the impedance of the line Z_0 which is proportional to the g factor of the spiral and on the number of turns.

During 1960's Cole [36] presented a circuit model of the nerves including the inductive effects of the small membrane currents.

In Table 1 a comparison between the Cole and the SCC inductances is proposed.

The expressions R' and G' for the SCC, related to the power loss per unit length due to the finite conductivity of the two spiral conductor strips and to the time-average power dissipated per unit length in the dielectric, respectively, are reported in Table 2 in a comparison with various types of transmission lines.

The inductance $L' \simeq 0$ [37] for the core-conductor model is negligible; (59) is then rewritten in the form

$$\begin{aligned} V &= \lambda^2\frac{\partial^2 V}{\partial z^2} - \tau\frac{\partial V}{\partial t}, \\ \lambda &= \frac{1}{\sqrt{R'G'}}, \\ \tau &= \frac{C'}{G'}, \\ T &= \frac{\tau\ell^2}{\lambda^2} = R'C'\ell^2, \end{aligned} \tag{80}$$

where λ and τ are called the cable space and time constants, respectively, while T is called the time per internodal distance ℓ [37].

Table 2: Transmission parameters for the MDSCC, MSSCC, the cylindrical coax, and the parallel plate lines.

	Double spiral coax	Single spiral coax	Cylindrical coax	Parallel plate
	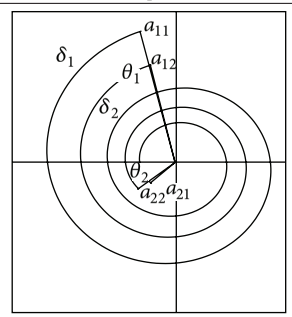	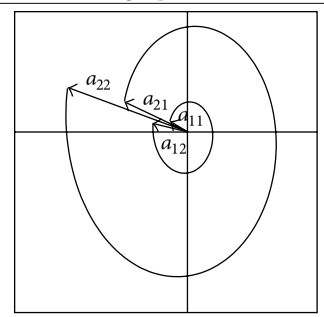	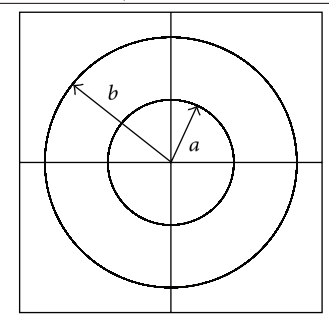	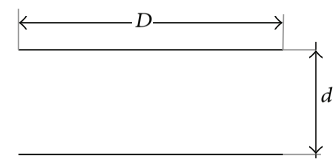
L'	$\frac{\mu}{g}\frac{1}{(((\theta_2-\theta_1)/(\delta_1-\delta_2))+((\theta_2-\theta_1-(2\pi/(1+g^2)))/(\delta_2-\delta_1+(2\pi g^2/(1+g^2)))))}$	$\mu\frac{ng}{1+g^2}$	$\frac{\mu}{2\pi}\ln\frac{b}{a}$	$\mu\frac{d}{D}$
C'	$\epsilon' gW\left(\frac{\theta_2-\theta_1}{\delta_1-\delta_2}+\frac{\theta_2-\theta_1-\left(2\pi/\left(1+g^2\right)\right)}{\delta_2-\delta_1+(2\pi g^2/(1+g^2))}\right)$	$\epsilon'\frac{(1+g^2)}{ng}$	$\epsilon'\frac{2\pi}{\ln b/a}$	$\epsilon'\frac{D}{d}$
R'	$\frac{R_S}{16g\sqrt{1+g^2}}\frac{1}{(\theta_2-\theta_1-(\pi/(1+g^2)))^2((1/(\delta_1-\delta_2))+1/(\delta_2-\delta_1)+(2\pi g^2/(1+g^2)))^2}$ $\times\left[\begin{array}{l}\frac{1}{a_{22}}\left(\frac{1}{(\delta_2-\delta_1)^2}+\frac{e^{(-(2g\pi/(1+g^2)))}}{(\delta_1-\delta_2+(2\pi g^2/(1+g^2)))^2}\right)\\ -\frac{1}{a_{21}}\left(\frac{1}{(\delta_2-\delta_1)^2}+\frac{1}{(\delta_1-\delta_2+(2\pi g^2/(1+g^2)))^2}\right)\\ +\frac{1}{a_{12}}\left(\frac{1}{(\delta_2-\delta_1)^2}+\frac{e^{-(4g\pi/(1+g^2))}}{(\delta_1-\delta_2+(2\pi g^2/(1+g^2)))^2}\right)\\ -\frac{1}{a_{11}}\left(\frac{1}{(\delta_2-\delta_1)^2}+\frac{e^{-(2g\pi/(1+g^2))}}{(\delta_1-\delta_2+(2\pi g^2/(1+g^2)))^2}\right)\end{array}\right]$ $a_{pq}=e^{(\delta_p/g)-g\theta_q},\quad p,q=1,2.$	$\frac{R_S}{8\pi^2\sqrt{1+g^2}}$ $\times\left[\begin{array}{l}\frac{1}{a_{11}}-\frac{1}{a_{12}}\\ +\frac{e^{-(2n\pi g^2/(1+g^2))}}{a_{21}}-\frac{e^{-(2n\pi g^2/(1+g^2))}}{a_{22}}\end{array}\right],$ $a_{pq}=e^{((\delta_1/g)-2g(p-q)\pi-g\theta_{i_p})}$ $p,q=1,2.$	$\frac{R_S}{2\pi}\left(\frac{1}{a}+\frac{1}{b}\right)$	$\frac{2R_S}{D}$
G'	$\omega\epsilon'' g\left(\frac{\theta_2-\theta_1}{(\delta_2-\delta_1)}+\frac{\theta_2-\theta_1-\left(2\pi/\left(1+g^2\right)\right)}{\delta_1-\delta_2+(2\pi g^2/(1+g^2))}\right)$	$\frac{\omega\epsilon''}{g}(1+g^2)$	$\frac{2\pi\omega\epsilon''}{\ln b/a}$	$\frac{\omega\epsilon'' D}{d}$

7. The Spiral Poynting Vector

On a matched spiral coaxial line the rms voltage V_0 is related to the total average power flow $P_z = (1/2)\int_{S_\perp} \vec{E}\times\vec{H}^*\cdot\hat{e}_z dS_\perp$ by

$$P_z = \begin{cases} \frac{1}{2}\int_{\delta_1}^{\delta_2}\int_{\theta_1}^{\theta_2}\vec{E}\times\vec{H}^*\cdot\hat{e}_z dS_\perp \\ \quad + \int_{\delta_2}^{\delta_1+2\pi g^2/(1+g^2)}\int_{\theta_1+2\pi/(1+g^2)}^{\theta_2}\vec{E}\times\vec{H}^*\cdot\hat{e}_z dS_\perp \\ = \frac{1}{2}\sqrt{\frac{\epsilon}{\mu}}gV_0^2\left(\frac{\theta_2-\theta_1}{\delta_2-\delta_1}+\frac{\theta_2-\theta_1-2\pi/\left(1+g^2\right)}{\delta_1-\delta_2+2\pi g^2/\left(1+g^2\right)}\right), \\ \qquad\qquad \text{double coax}, \\ \frac{1}{2}\int_{\delta_1}^{\delta_1+2n\pi g^2/(1+g^2)}\int_{\theta_1}^{\theta_2}\vec{E}\times\vec{H}^*\cdot\hat{e}_z dS_\perp \\ = \frac{1}{\eta}\frac{1+g^2}{2gn}V_0^2, \qquad \text{single coax}, \end{cases} \tag{81}$$

where the infinitesimal cross section is $dS_\perp \equiv \|d\vec{S}_{\delta\theta}\|$ of (20).

As the g factor decreases, for example in the evolution of the Schwann's cell around the axon, progressively a higher number of spiral turns are required to yield the same value of transmitted power. Likewise, overcoming the power threshold in neural networks may provoke nerve inflammation and disorders or vice versa an amount of power below the natural required level could cause the neural signal to be blocked.

In order to change the transmitted power, the neural system can modify the number n of turns or the g factor.

Peters and Webster [27, 38, 39] showed that the angles subtended at the centre of the axon between the internal mesaxon and outer tongue of cytoplasm obey a precise statistic, that is, in about 75% of the mature myelin sheaths they examined the angle that lied within the same quadrant. This work refines the coaxial model for myelinated nerves introducing the spiral geometry and gives an explanation for the *Peters quadrant mystery* [38]. The surprising tendency for the start and finish of the myelin spiral to occur close together, according to this spiral coaxial model, comes out from the need of handling power throughout the nervous system.

In fact, the Poynting vector of (81) depends linearly on the Peters angle β_p which represents a finicky control of the power delivered along the myelinated nerves. A malformation of the Peters angle causes higher/lower power to be transmitted in the neural networks with respect to the required normal level.

8. Conclusions

In this paper two types of metal spiral coaxial cables have been proposed, the MSCC and the MDSCC.

A generalization of the *Schwarz-Christoffel* [40] conformal mapping was used to map the transverse section of the MSCC into a rectangle and to find the solution to its equivalent electrostatic *Laplace's equation*.

The fundamental TEM wave propagating along the MSCC has been determined together with the impedances of the line.

Comparisons of the MSCC with the classical cylindrical coax as well as with the hollow polar waveguide have been done.

The myelinated nerves, whose elm model is still based on the core-conductor theory, are analyzed by using the spiral coaxial model and their spiral geometrical factors are precisely related to the electrical impedances and propagating elm fields. The spiral model could be used to better analyze the neurodegenerative diseases, which are strictly connected to the geometrical malformations of the myelin bundles.

The MDSCC has many advantages compared to the cylindrical coaxial cable because it can be made multiturn, thus distributing the energy over a larger area and protecting the small signals from interference due to external electric fields.

The MSCC could have many interesting applications in the field of video and data transmission, as well as for sensing, instrumentation/control, communication equipment, and plasmonic nanostructure at optical wavelength.

Appendix

Spiral Generalization of the *Schwarz-Christoffel* Conformal Mapping

We define a spiral conformal coordinate system (u, v) as one as specified by a complex analytic function

$$w = u + iv, \quad w = f(z), \tag{A.1}$$

$$f(z) = A_0\int_{z_0}^{z}\frac{1}{\zeta}d\zeta, \quad A_0 = 1 - ig,\ z_0 \neq 0, \tag{A.2}$$

where $g \in \mathbb{R}$ is a constant [40] and the function $f(z)$ is a generalization of the well-known holomorphic Schwarz-Christoffel [41] formula:

$$W(z) = A_0\int_{z_0}^{z}\prod_{k=1}^{n}(\zeta-\zeta_k)^{-\alpha_k/\pi}d\zeta + B_0 \quad A_0, B_0 \in \mathbb{C}, \tag{A.3}$$

because for $\alpha_1 = \pi, \zeta_1 = 0$ and $\alpha_k = 0, \forall k > 1, \zeta_k = 0, \forall k \geq 1$, the two formulas of (A.2) and (A.3) are identical.

Since $f(z)$ is holomorphic the derivative $f'(z)$ exists and it is independent of direction.

For $g = 0$ or $A_0 \in \mathbb{R}$, the spiral conformal mapping of (A.1)-(A.2) coincides with the polar mapping (see [18] page 135); the elm propagation along the circular waveguide is then included in the theoretical treatment of this paper as a particular case.

In terms of cartesian (x, y) or polar (r, φ) coordinates

$$z = x + iy = re^{i\varphi}. \tag{A.4}$$

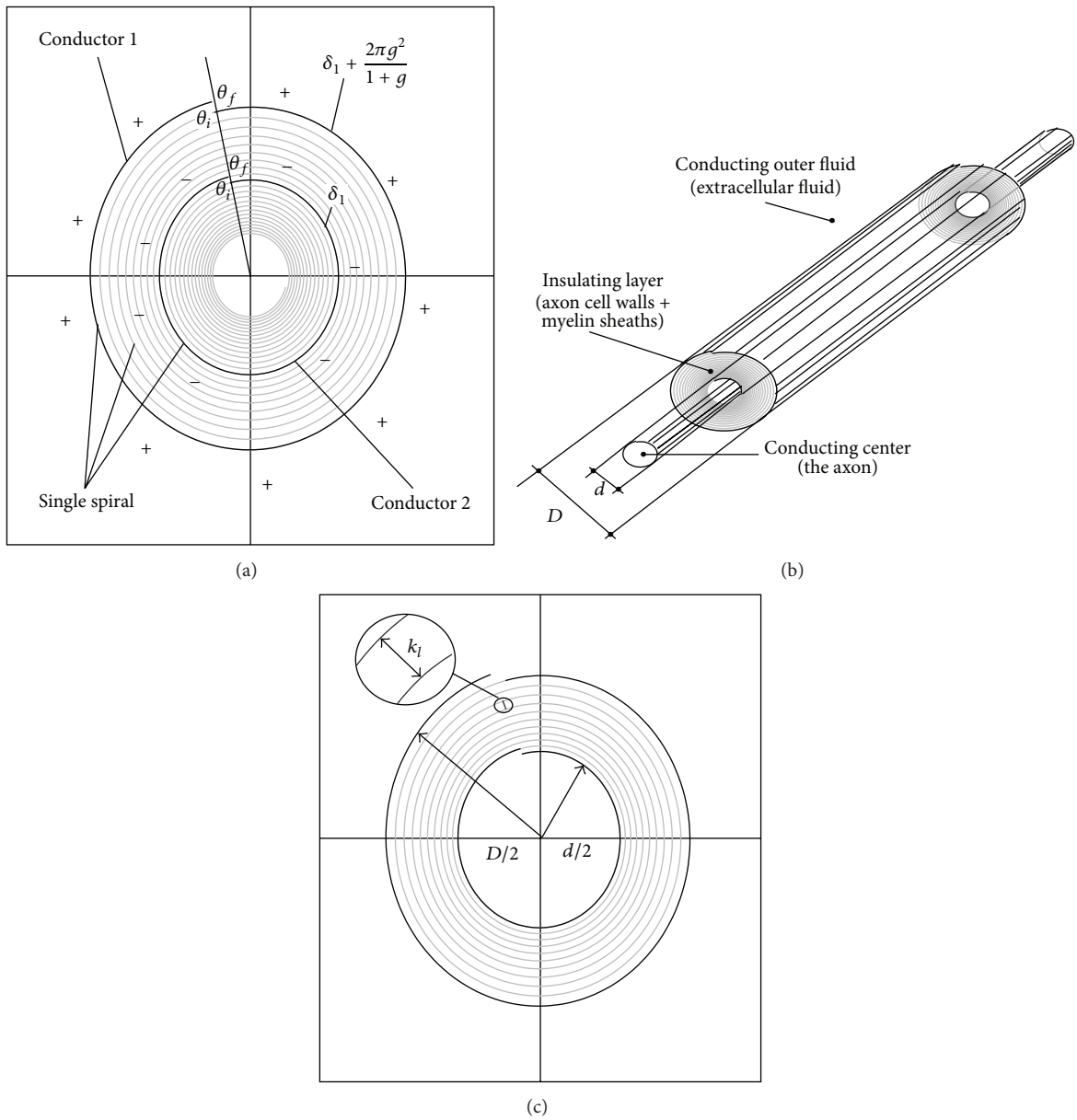

Figure 6: SSCC (a) transverse section, (b) longitudinal view, and (c) the myelin sheaths.

Substituting (A.2) into (A.1) we obtain

$$u + iv = (1 - ig)\log z + K = f(z). \tag{A.5}$$

The value of the constant K represents the phase of the transformation and is related to $z_0 = e^{-K}$.

In order to study the spiral coaxial cable a further normalization of the angles u and v is introduced:

$$u + iv = \frac{1+g^2}{g}\delta + i\left(1+g^2\right)\theta. \tag{A.6}$$

θ, δ are the two normalized variables. Using (A.1), (A.4), (A.6), and

$$w = (1 - ig)(\log r + i\varphi) + K \tag{A.7}$$

we obtain the direct complex spiral coordinate transformation; that is,

$$z = e^{\delta/g - g\theta + i(\delta+\theta)}, \tag{A.8}$$

where $K = 0$.

If $g = 0$ and $K = 0$ the two variables u, v coincide with the polar variables $\ln r$, φ (see [18] page 135).

The transverse arclength in cartesian or polar coordinates becomes

$$(d\ell)^2 = |dz|^2 = (dx)^2 + (dy)^2 = (dr)^2 + (rd\varphi)^2, \tag{A.9}$$

where

$$|dz|^2 = \left|f'(z)\right|^{-2} |dw|^2, \tag{A.10}$$

or in conformal coordinates

$$(d\ell)^2 = |s|^2 \left((du)^2 + (dv)^2\right), \quad |s| \equiv \frac{1}{|f'(z)|}, \tag{A.11}$$

where the scale factor is the inverse of the modulus of the derivative of the function; that is,

$$f'(z) = \frac{1 - ig}{z}. \tag{A.12}$$

Substituting (A.6) into (A.11) we have

$$(d\ell)^2 = |S|^2 \left(\left(\frac{d\delta}{g}\right)^2 + (d\theta)^2\right), \tag{A.13}$$

where

$$|S| = \left(1 + g^2\right)|s|. \tag{A.14}$$

Although the scale factors of the variables δ and θ are not equal, their normalized coordinate system is orthogonal and the potential satisfies the same differential equation that it does in the x, y coordinates [18]. By using the variables u and v of the original conformal mapping presented in [40], for which the scale factors are identical, it is possible to obtain exactly the same results of this paper.

The complex variable $z = x + iy$ here used to describe the spiral conformal mapping is not the same variable "z" that represents the longitudinal coordinate of the waveguide. Nevertheless, the general treatment of the elm propagation in waveguide [28] and Maxwell's differential operators are separated into the longitudinal and the transverse parts.

Conflict of Interests

The author declares that there is no conflict of interests regarding the publication of this paper.

References

[1] O. Heaviside, *Electromagnetic Theory*, vol. 1, Dover, New York, NY, USA, 1950.

[2] D. M. Pozar, *Microwave Engineering*, John Wiley & Sons, 4th edition, 2011.

[3] A. S. Khan, *Microwave Engineering: Concepts and Fundamentals*, CRC Press, New York, NY, USA, 2014.

[4] S. Ramo, J. R. Whinnery, and T. Van Duzer, *Fields and Waves in Communication Electronics*, John Wiley & Sons, 3rd edition, 1993.

[5] G. Lifante, *Integrated Photonics: Fundamentals*, John Wiley & Sons, Chichester, UK, 2003.

[6] C. H. Lee, *Microwave Photonics*, CRC Press, New York, NY, USA, 2006.

[7] R. de Waele, S. P. Burgos, A. Polman, and H. A. Atwater, "Plasmon dispersion in coaxial waveguides from single-cavity optical transmission measurements," *Nano Letters*, vol. 9, no. 8, pp. 2832–2837, 2009.

[8] M. S. Kushwaha and B. D. Rouhani, "Surface plasmons in coaxial metamaterial cables," *Modern Physics Letters B*, vol. 27, no. 17, Article ID 1330013, 2013.

[9] J.-C. Weeber, A. Dereux, C. Girard, J. R. Krenn, and J.-P. Goudonnet, "Plasmon polaritons of metallic nanowires for controlling submicron propagation of light," *Physical Review B: Condensed Matter and Materials Physics*, vol. 60, no. 12, pp. 9061–9068, 1999.

[10] H. Regneault, J. M. Lourtioz, and C. Delalande, *Levenson Nanophotonics*, John Wiley & Sons, New York, NY, USA, 2010.

[11] G. Veronis, Z. Yu, S. Kocaba, D. A. B. Miller, M. L. Brongersma, and S. Fan, "Metal-dielectric-metal plasmonic wave guide devices for manipulating light at the nanoscale," *Chinese Optics Letters*, vol. 7, no. 4, pp. 302–308, 2009.

[12] M. L. Brongersma, J. W. Hartman, and H. A. Atwater, "Electromagnetic energy transfer and switching in nanoparticle chain arrays below the diffraction limit," *Physical Review B—Condensed Matter and Materials Physics*, vol. 62, no. 24, pp. R16356–R16359, 2000.

[13] T. W. Ebbesen, H. J. Lezec, H. F. Ghaemi, T. Thio, and P. A. Wolff, "Extraordinary optical transmission through sub-wavelenght hole arrays," *Nature*, vol. 391, no. 6668, pp. 667–669, 1998.

[14] G. Boisde and A. Harmer, *Chemical and Biochemical Sensing with Optical Fibers and Waveguides*, Arthech House, Boston, Mass, USA, 1996.

[15] A. V. Zayats, I. I. Smolyaninov, and A. A. Maradudin, "Nano-optics of surface plasmon polaritons," *Physics Reports*, vol. 408, no. 3-4, pp. 131–314, 2005.

[16] J. A. Stratton, *Electromagnetic Theory*, McGraw-Hill, New York, NY, USA, 1941.

[17] R. E. Collin, *Foundations for Microwave Engineering*, IEEE Press, Wiley Interscience, New York, NY, USA, 2nd edition, 2001.

[18] R. E. Collin, *Field Theory of Guided Waves*, Mc-Graw Hill, New York, NY, USA, 1960.

[19] L. Rayleigh, "On the passage of electric waves through tubes," *Philosophical Magazine*, vol. 43, no. 261, pp. 125–132, 1897.

[20] I. M. Fabbri, A. Lauto, and A. Lucianetti, "A spiral index profile for high power optical fibers," *Journal of Optics A: Pure and Applied Optics*, vol. 9, no. 11, pp. 963–971, 2007.

[21] I. M. Fabbri, A. Lucianetti, and I. Krasikov, "On a Sturm Liouville periodic boundary values problem," *Integral Transforms and Special Functions*, vol. 20, no. 5-6, pp. 353–364, 2009.

[22] K. Guven, E. Saenz, R. Gonzalo, E. Ozbay, and S. Tretyakov, "Electromagnetic cloaking with canonical spiral inclusions," *New Journal of Physics*, vol. 10, Article ID 115037, 2008.

[23] W. T. Kelvin, "On the theory of the electric telegraph," *Proceedings of the Royal Society of London*, vol. 7, pp. 382–389, 1855.

[24] W. Rall, "Core conductor theory and cable properties of neurons," in *Handbook of Physiology, the Nervous System, Cellular Biology of Neurons*, John Wiley & Sons, New York, NY, USA, 2011.

[25] A. H. Buck, *Reference Handbook of the Medical Sciences*, vol. 3 of *edited by A. H. Buck*, Book on Demand, New York, NY, USA, 1901.

[26] A. L. Hodgkin and A. F. Huxley, "A quantitative description of membrane current and its application to conduction and excitation in nerve," *The Journal of Physiology*, vol. 117, no. 4, pp. 500–544, 1952.

[27] A. Peters, "Further observations on the structure of myelin sheaths in the central nervous system," *The Journal of Cell Biology*, vol. 20, pp. 281–296, 1964.

[28] N. Marcuvitz, *Waveguide Handbook*, Peter Peregrinus, New York, NY, USA, 1986.

[29] I. Boscolo and I. M. Fabbri, "A tunable bragg cavity for an efficient millimeter FEL driven by electrostatic accelerators," *Applied Physics B Photophysics and Laser Chemistry*, vol. 57, no. 3, pp. 217–225, 1993.

[30] J. D. Jackson, *Classical Electrodynamics*, John Wiley & Sons, New York, NY, USA, 1962.

[31] G. Mie, "Beiträge zur Optik trüber Medien, speziell kolloidaler Metallösungen," *Annalen der Physik*, vol. 330, no. 3, pp. 337–445, 1908, English translated by B. Crossland, Contributions to the optics of turbid media, particularly of colloidal metal solutions, Nasa Royal Aircraft Establishment no. 1873, 1976.

[32] M. Born and E. Wolf, *Principles of Optics: Electromagnetic Theory of Propagation*, Cambridge University Press, Cambridge,UK, 1999.

[33] V. M. Agranovich and D. L. Mills, Eds., *Surface Polaritons*, North-Holland, Amsterdam, The Netherlands, 1982.

[34] Y. Min, K. Kristiansen, J. M. Boggs, C. Husted, J. A. Zasadzinski, and J. Israelachvili, "Interaction forces and adhesion of supported myelin lipid bilayers modulated by myelin basic protein," *Proceedings of the National Academy of Sciences of the United States of America*, vol. 106, no. 9, pp. 3154–3159, 2009.

[35] C. H. Berthold, I. Nilsson, and M. Rydmark, "Axon diameter and myelin sheath thickness in nerve fibres of the ventral spinal root of the seventh lumbar nerve of the adult and developing cat," *Journal of Anatomy*, vol. 136, no. 3, pp. 483–508, 1983.

[36] K. Cole, *Membranes, Ions and Impulses: A Chapter of Classical Biophysics*, University of California Press, Los Angeles, Calif, USA, 1968.

[37] A. F. Huxley and R. Stampfli, "Evidence for saltatory conduction in peripheral myelinated nerve fibres," *The Journal of Physiology*, vol. 108, no. 3, pp. 315–339, 1949.

[38] R. R. Traill, *Strange Regularities in the Geometry of Myelin Nerve-Insulation—A Possible Single Cause*, Ondwelle Short Monograph no. 1, 2005.

[39] H. D. Webster, "The geometry of peripheral myelin sheaths during their formation and growth in rat sciatic nerves," *The Journal of Cell Biology*, vol. 48, no. 2, pp. 348–367, 1971.

[40] L. M. B. Campos and P. J. S. Gil, "On spiral coordinates with application to wave propagation," *Journal of Fluid Mechanics*, vol. 301, pp. 153–173, 1995.

[41] Z. Nehari, *Conformal Mapping*, Dover, New York, NY, USA, 1975.